

Advancing High-Energy Solid-State Batteries with High-Entropy NASICON-type Solid Electrolytes

Asish Kumar Das^a, Pratiksha Gami^a, Hari Narayanan Vasavan^a, Samriddhi Saxena^a, Neha Dagar^a, Sonia Deswal^b, Pradeep Kumar^b, Sunil Kumar^{a,*}

^aDepartment of Metallurgical Engineering and Materials Science, Indian Institute of Technology Indore, Simrol, 453552, India

^bSchool of Physical Sciences, Indian Institute of Technology Mandi, Himachal Pradesh, 175005, India

*Corresponding author E-mail: sunil@iiti.ac.in

Abstract:

Herein, we have developed a *High-Entropy* ($\sim 1.52 R$, calculated at M-site) lithium-stuffed NASICON-type solid electrolyte $[\text{Li}_{1.3}\text{Sn}_{1.7/3}\text{Zr}_{1.7/3}\text{Ti}_{1.7/3}\text{Al}_{0.1}\text{Sc}_{0.1}\text{Y}_{0.1}(\text{PO}_4)_3]$ (HE-LSZT) with a total (grain + grain-boundary) ionic conductivity of $\sim 1.42 \times 10^{-4} \text{ S cm}^{-1}$ (highest reported among NASICONs containing Zr-Sn-Ti) and a low activation energy of $\sim 0.33 \text{ eV}$ with a relative density of *Conventionally Sintered* pellet $\sim 94\%$. Symmetric cells with a PVDF-HFP/LiTFSI buffer layer showed stable performance for 500 cycles at 0.2 mA cm^{-2} without short-circuiting. Full cells with LiFePO_4 retained $\sim 99\%$ capacity after 100 cycles at 1C, while those with NMC811 delivered $\sim 140 \text{ mAh g}^{-1}$ at C/3.

Keywords: *Solid electrolytes; ionic conductivity; high entropy; NASICON-type, lithium-ion.*

As the demand for safer and more efficient energy solutions grows, transitioning to solid electrolytes becomes increasingly imperative because of traditional liquid electrolytes' flammability and leakage issues. Solid ceramic electrolytes not only offer enhanced safety but also enable the application of cathodes with high redox potentials and Li anodes (lowest redox potential of ~ 0 V vs. Li/Li⁺ and highest specific capacity ~ 3860 mAh g⁻¹), paving the way for batteries with considerable higher energy densities.¹⁻⁴ This has reignited efforts to develop materials that facilitate rapid lithium-ion conduction.

Among the leading candidates for next-generation rechargeable lithium batteries are thiophosphates (Li₂S-P₂S₅), NASICON-framework materials, and garnets.⁵⁻¹⁰ Thiophosphates boast excellent total (grain + grain boundary) conductivity ($> 10^{-3}$ S cm⁻¹ at 25 °C), but their electrochemical stability with cathode and anode materials, as well as their stability under ambient conditions, is lacking.¹¹ Conversely, NASICONs, though offering lower ionic conductivity, exhibit better stability in ambient conditions and with commonly used cathode materials. This has led to extensive research into NASICON-type compounds (Li_xM₂(PO₄)₃ phases, M representing main group or transition metal elements like Ge, Ti, etc.) to achieve room temperature lithium conductivity exceeding 10⁻⁴ S cm⁻¹.¹²⁻¹⁴ NASICON (Sodium Super Ionic Conductor) structures are characterized by their unique three-dimensional framework, consisting of corner-sharing MO₆ octahedra and PO₄ tetrahedra. This arrangement forms interstitial sites and channels that facilitate rapid ionic conduction.

Unlike in Na-polymorphs, the rhombohedral phases show superior conductivity to other NASICON-based Li-conducting structures. Li⁺ conduction in these materials is further enhanced by substituting aliovalent cations, which create interstitials and tune the bottleneck size for lithium-ion migration in the crystal structure.¹⁵⁻¹⁷ Furthermore, large anisotropic lattice contraction during

the cooling cycle after sintering causes cracks in these materials. Ultimately, the total conductivity of the solid electrolyte is overwhelmed by the sluggish lithium-ion conduction across the cracks.¹⁸ Further, a few reports demonstrated that adding ortho-valent elements like Al³⁺ improves the ionic conductivity and acts as a sintering additive with an improved relative density of the polycrystalline ceramics.¹⁵

Recently, the introduction of disorderliness in solid electrolyte materials has garnered much attention due to the stabilization of highly lithium-ion conductive crystal structures and improved electrochemical stability.¹⁹⁻²⁴ Very few studies on high entropy (HE), with configurational entropy > 1.5R, NASICON-type Li-ion conducting materials exist. Zeng et al. demonstrated the impact of local distortions in a HE Li(TiZrSnHf)₂(PO₄)₃ to obtain a total conductivity of ~ 2.2 × 10⁻⁵ S cm⁻¹ (85% dense pellet), which was much higher than their single metal analogues.²⁵ In addition, the spark plasma sintering (SPS) in a vacuum or Ar- atmosphere is not preferred for the solid electrolytes containing elements like Ti, Ge, etc., as Ti and Ge change their oxidation state from +4 to +3.²⁶ So, it is imperative to develop solid electrolytes that can attain a high relative density by conventional sintering method to be employed as a solid electrolyte in solid-state lithium metal batteries. To our knowledge, no HE NASICON-type solid electrolyte has been reported with aliovalent substitution at the M-site.

In this study, the structure and electrochemical behavior of a *High-Entropy* (~ 1.52R),

$$\begin{aligned}
 S_{config} \text{ at } M - \text{site} &= -R \left[\sum_{i=1}^N x_i \ln x_i \right]_{M\text{-site}} \\
 &= -R \left(3 \times \left[\frac{(1.7/3)}{2} \times \ln \left[\frac{(1.7/3)}{2} \right] \right) + \left(3 \times \left[\frac{(0.1)}{2} \times \ln \left[\frac{(0.1)}{2} \right] \right) \right)
 \end{aligned}$$

lithium-stuffed NASICON solid electrolyte Li_{1.3}Sn_{1.7/3}Zr_{1.7/3}Ti_{1.7/3}Al_{0.1}Sc_{0.1}Y_{0.1}(PO₄)₃ (HE-LSZT) with a total (grain + grain-boundary) ionic conductivity of ~ 1.42 × 10⁻⁴ S cm⁻¹ and a low activation

energy barrier of ~ 0.33 eV with a relative density of $\sim 94\%$ are reported. It has the highest conductivity reported for germanium-free NASICON-based Li-solid electrolytes with the least Ti content in the composition. A PVDF-HFP/LiTFSI buffer layer was used to avoid lithium-metal contact with the HE-LSZT solid electrolyte. At the same time, lithium full cells were fabricated with NMC811 and LiFePO₄ as the positive electrode materials.

The crystal structure of Li_{1.3}Sn_{1.7/3}Zr_{1.7/3}Ti_{1.7/3}Al_{0.1}Sc_{0.1}Y_{0.1}(PO₄)₃ (HE-LSZT) synthesized at 1200 °C through solid-state reaction route was investigated through Rietveld refinement of the powder XRD data. The XRD data was modeled with a 6-order polynomial background and PV-II peak type along with the rhombohedral $R\bar{3}c$ (Space Group number: 167), as presented in Figure 1(a) and the goodness of the fit was found to be ~ 1.98 .

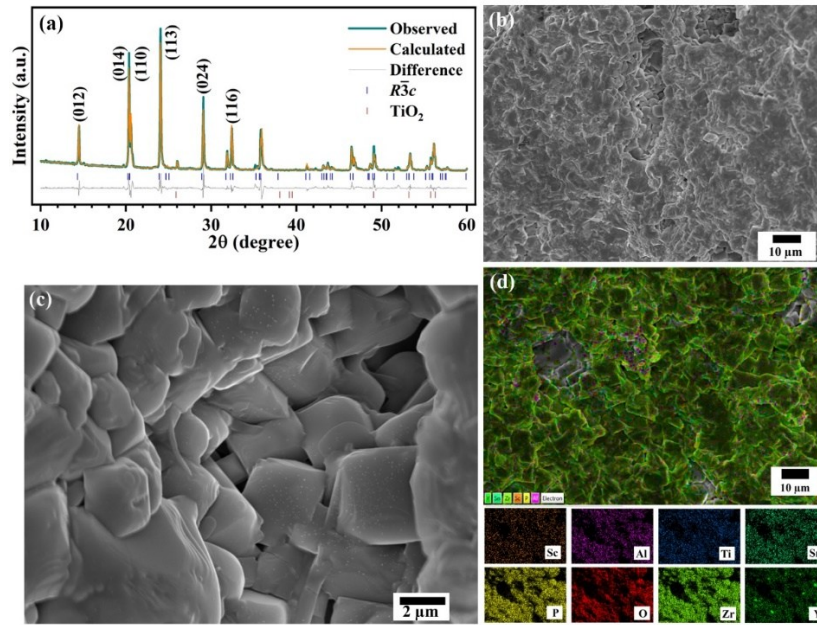


Figure 1: (a) Room temperature powder x-ray diffraction data (dark cyan line) for HE-LSZT sample calcined at 1200 °C for 12 h. The calculated pattern obtained from the refinement is shown as an orange line; the profile difference is depicted with a grey line. The calculated Bragg positions for HE-LSZT and TiO₂ are indicated by royal and wine vertical bars at the bottom, respectively. (b) SEM image of the sintered HE-LSZT ceramic electrolyte at lower magnification. (c) SEM image of the sintered HE-LSZT ceramic electrolyte at higher magnification. (d) EDS of the solid electrolyte along with the elemental distributions of Sc, Al, Ti, Sn, P, O, Zr, and Y.

The rhombohedral phase was most prominent, with a low-intensity tetragonal anatase TiO_2 impurity peak with a phase fraction of $< 2\%$. The lattice parameters and volume were determined to be $a = 8.6821(3) \text{ \AA}$, $c = 21.6174(14) \text{ \AA}$, and $V = 1411.17(14) \text{ \AA}^3$, respectively, with a crystal density of $\sim 3.21 \text{ g cm}^{-3}$. 36f sites were assigned to the additional lithium-ions due to the introduction of aliovalent atoms, and lithium occupancies at 6b and 36f Wyckoff positions were varied during refinement. Ab initio, molecular dynamics studies have identified the "pushing-out" mechanism as the reason for the high ionic conductivity seen in Li-rich NASICON-type electrolytes.²⁷ This mechanism occurs when an additional lithium-ion is introduced, causing strong electrostatic repulsion among the positively charged lithium ions. The repulsive force compels the new lithium-ion to move away from its neighboring ions, overcoming the binding energy that usually holds a nearby lithium ion in place. This displacement sets off a domino effect where the displaced ion is similarly repelled by its neighbors, effectively pushing it out of its initial position.^{27, 28}

Figures 1(b) and 1(c) depict the high densification of the sintered ceramic sample at $1200 \text{ }^\circ\text{C}$ (12h). Archimedes' method determined the relative density of $\sim 94.5\%$ in the HE-LSZT sample, which is higher or comparable to other NASICON-type materials reported in the literature.^{17, 18, 29, 30} The successful substitution of various elements at the M-site in the HE-LSZT sample was confirmed by the uniform elemental distribution, as shown in EDS mapping (Figure 1(d)). Various studies demonstrated that aliovalent substitutions like Al, Sc, and Y improve the relative density; in addition, in the HE-LSZT sample, the disorderliness may contribute to sintering. Also, the absence of any visible inter-grain or intra-grain cracks would facilitate better lithium-ion conduction. As reported earlier, the high anisotropy in thermal expansion of lattice parameters a and c causes

inter/intra-grain cracks during cooling in the sintering process. Introducing high entropy in the HE-LSZT may decrease the degree of anisotropic thermal expansion, expediting a crack-free sintered solid electrolyte sample, which can impede the Li-dendrite-guided micro short-circuits.

The impedance measurements were performed to measure the conductivity of the synthesized sample at different temperatures. Figures 2(a) & S1 present the Nyquist plots (experimental and fitted data) at different temperatures within a frequency range of 1 Hz – 1 MHz and with a sinusoidal input signal of 0.1 V amplitude. Figure 2(a) inset is the equivalent circuit to model the impedance data, where Q and R stand for constant phase and resistance elements.

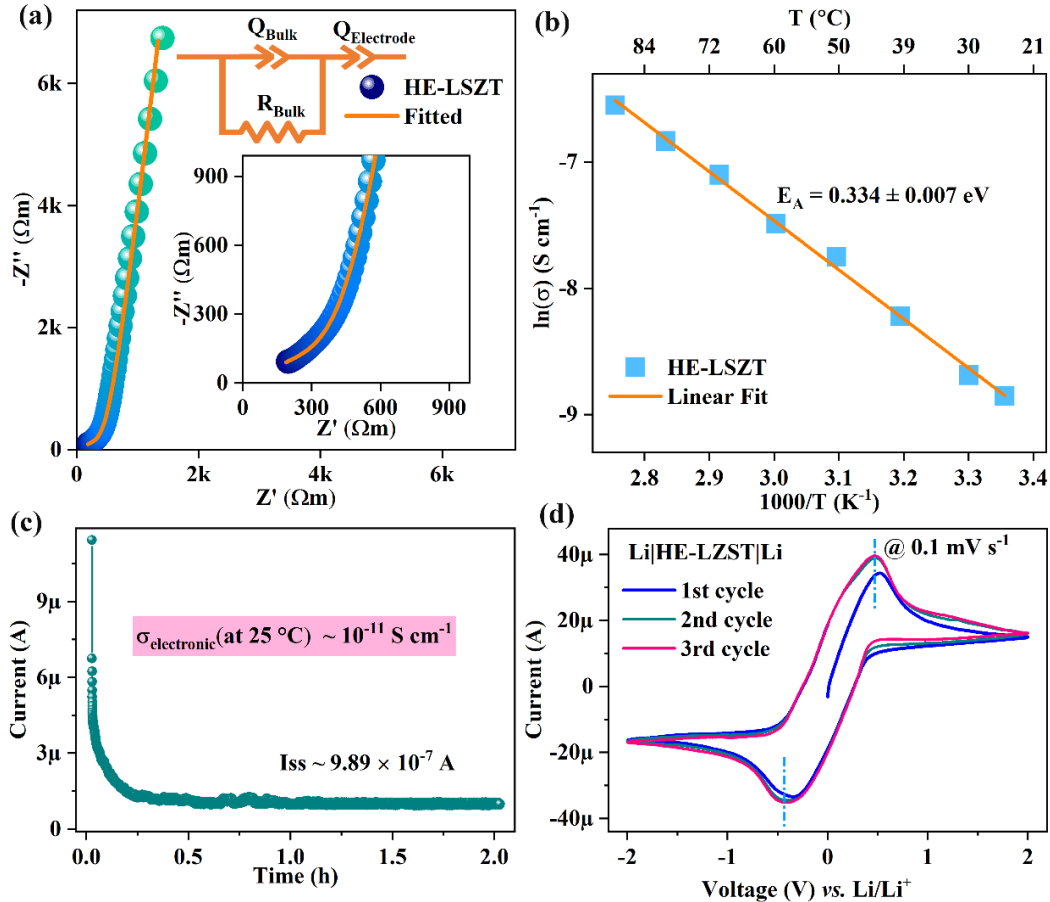


Figure 2: (a) Room temperature Nyquist plot of HE-LSZT sample (inset displays the equivalent circuit used for fitting the impedance data). The scattered spheres and the orange line represent the experimental and fitted data, respectively. (b) Linear fitting of temperature-dependent conductivities of HE-LSZT sample using the Arrhenius equation. (c) DC voltage polarization measurement on the Ag|HE-LSZT|Ag configuration. (d) Cyclic voltammetry curves for Li|HE-LSZT|Li cell at a scan rate of 0.1 mV s^{-1} at room temperature.

The grain and grain-boundary relaxations are not separately visible in the Nyquist plot. The partial semicircular arc in the high-frequency region is modeled by the parallel connection of Q_{Bulk} and R_{Bulk} , where the tail feature at the low-frequency regime denotes the capacitive behavior at the sample & ion-blocking silver electrode interface. A constant phase element ($Q_{\text{Electrode}}$) was used instead of a pure capacitor due to the non-uniform interface. The conductivity of HE-LSZT at room temperature was determined to be $1.42 \times 10^{-4} \text{ S cm}^{-1}$ with a low activation energy of $\sim 0.334 \pm 0.007 \text{ eV}$, calculated using the Arrhenius equation given by:

$$\sigma(T) = \sigma_0 e^{-\frac{E_a}{k_B T}} \quad (1)$$

where T denotes the absolute temperature, σ_0 and E_a represent the pre-exponential factor and activation energy, respectively (Figure 2(b)). The very low energy barrier of the high-entropy HE-LSZT sample, as compared to other NASICON-type materials reported in the literature, is attributed to the flattening of energy landscapes resulting from the introduction of various elements and additional lithium redistribution at 36f sites in the unit cell.^{17, 18, 31}

A DC polarization test was employed on the Ag|HE-LSZT|Ag under 0.2 V to separate the electronic conduction from the total conductivity of the sample (Figure 2(c)). The electronic conductivity ($\sigma_{\text{electronic}}$) of the sample was calculated to be around $\sim 10^{-11} \text{ S cm}^{-1}$ using the sample's dimensions, applied voltage, and steady-state current. Li-ion transference number is calculated using the formula $t_{\text{Li}^+} = 1 - \frac{\sigma_{\text{electronic}}}{\sigma_{\text{bulk}}} \sim 0.999$. Thus, the conductivity of the HE-LSZT sample is mostly from Li-ion conduction only. The very low electronic conductivity of the sample alleviates one of the concerning causes for lithium dendrite propagation in the solid electrolyte, along with high columbic efficiency, which propels the long cycling stability of the solid-state battery.

To verify the Li^+ migration in the HE-LSZT sample, the cyclic voltammetry test was carried out on the $\text{Li}|\text{HE-LSZT}|\text{Li}$ cell without a buffer layer (Li acting as both positive and negative electrodes). Figure 2(d) presents the result of CV performed at 0.1 mV s^{-1} for 3 cycles in the voltage window of -2 V to $+2 \text{ V}$. The redox peaks around $+0.47 \text{ V}$ and -0.43 V affirmed Li^+ mobility through the solid electrolyte HE-LSZT. The high polarization voltage may indicate improper physical contact or the highly resistive passivation layer formed at the solid electrolyte/lithium metal interface. Further, the upper oxidation voltage value of the electrochemical stability window was determined to be $\sim 5.2 \text{ V}$ using linear sweep voltammetry on $\text{Li}|\text{HE-LSZT}|\text{Ag}$ cells (Figure S2).

The XPS data for various elements was collected from the as-sintered electrolyte sample before and after the lithium metal contact. As shown in Figure 3(a), no discernible change like asymmetry or splitting in the XPS plot of various elements (Zr, Sn, Ti, Al, Sc, Y) was observed, indicating the chemical stability of the synthesized electrolyte in contact with lithium metal. This suggests that infusing disorderliness in the crystal structure avoids the possible chemical reduction of elements present at the M-site in the HE-LSZT solid electrolyte in physical contact with lithium metal. Accordingly, the synthesized electrolyte can be used as an electrolyte if intimate contact with both the cathode and anode can be designed. In this work, a buffer layer of P(VDF-HFP)-LiTFSI at the lithium metal interface, whereas a liquid electrolyte at the cathode side was used for proper physical contact.

The EIS data were recorded to evaluate the interfaces in $\text{Li}|\text{HE-LSZT}|\text{Li}$ symmetric cells with and without P(VDF-HFP)-LiTFSI buffer layer and presented in Figure 3(b) (the inset depicts the equivalent circuit used for modeling). The high-frequency intercept indicates the solid electrolyte's resistance, where the semi-circular feature in the mid-frequency regime presents the interface

resistance, and the tail feature in low frequencies appears due to lithium blocking at the current collector. The Nyquist plots for the Li symmetric cells without a buffer layer show a bigger semicircular arc in the mid-frequency region, indicating a high charge transfer resistance across the two interfaces. In contrast, the presence of a buffer layer at the electrode-electrolyte interface exhibited a much smaller arc at the same frequency, suggesting a lower interface resistance and a much-improved interface contact.

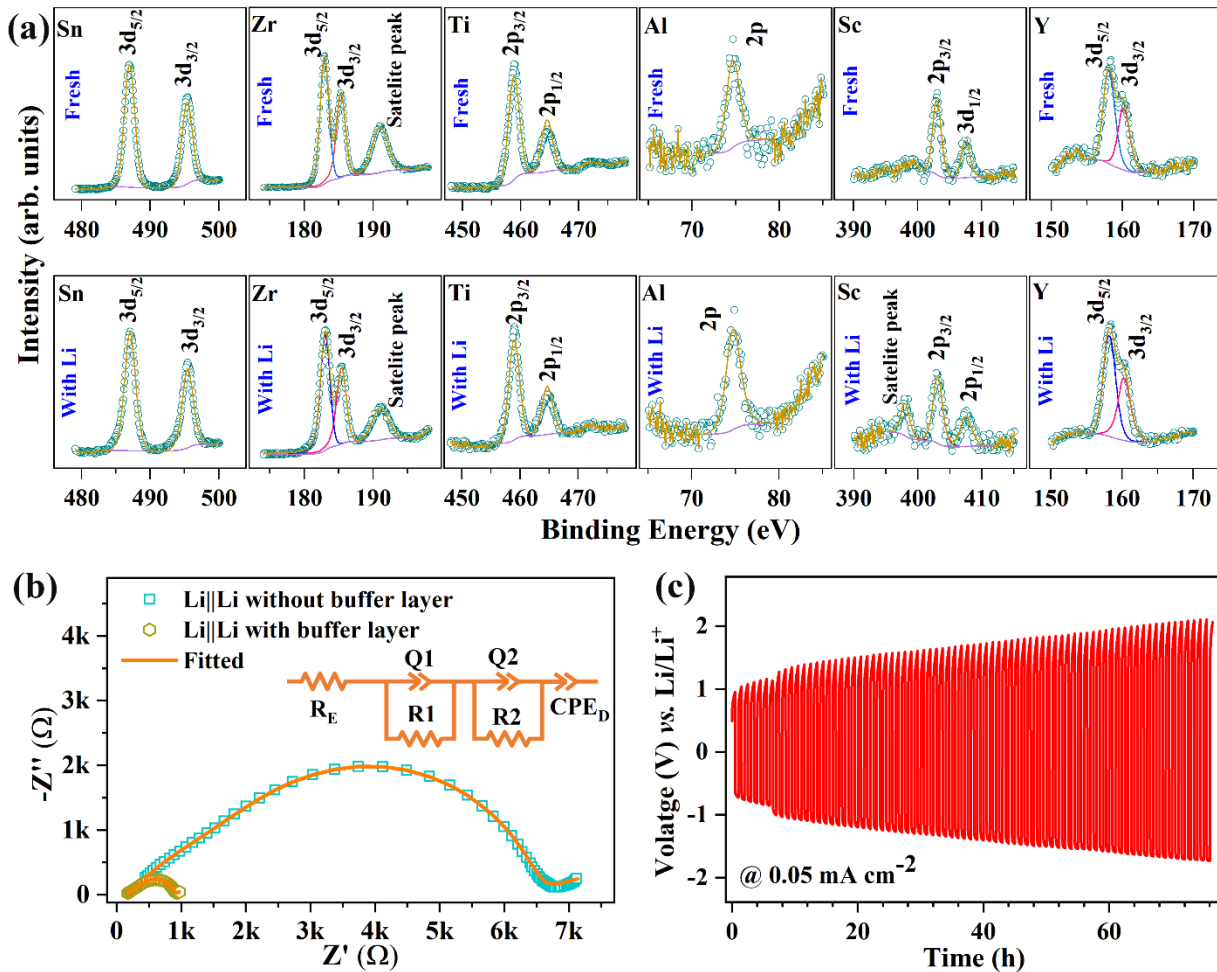


Figure 3: (a) The orange and dark cyan XPS curves of Sn 3d, Zr 3d, Ti 2p, Al 2p, Sc 2p, and Y 3d were obtained from the solid electrolyte before and after the contact with lithium metal for 24 h at room temperature, respectively. (b) Room temperature Nyquist plot of Li|HE-LSZT|Li cells without buffer layer and with buffer layer. (inset displays the equivalent circuit used for fitting the impedance data). The scattered symbol and the pink line represent the experimental and fitted data, respectively. (c) The room

temperature galvanostatic curves indicate lithium plating-stripping in Li|HE-LSZT|Li cell without buffer layer at a current of 0.05 mA cm⁻² for 75 h.

The high resistance in the cells with the ceramic solid electrolyte is attributed to the uneven interfacial contact, which can cause local current hot spots leading to dendrite formation during charging-discharging.³²⁻³⁴ The lithium plating-stripping voltage profile of Li|HE-LSZT|Li cells without any buffer layer at different current densities is presented in Figure S3. In Figure 3(c), a steady increase in the overpotential (overpotentials at 0 h & 75 h ~ 1 V & ~ 2 V, respectively) during lithium plating-stripping of Li|HE-LSZT|Li cells without any buffer layer was observed at a low current density of 0.05 mA cm⁻². Further, lithium plating-stripping was tested on the symmetric lithium cell Li|HE-LSZT|Li with a buffer layer at different current densities, and the critical current density was found to be ~ 0.6 mA cm⁻² (Figure 4(a)). The lithium plating-stripping potential increased steadily as the current density increased along with the diminishing flatness of the voltage profile. At 0.8 mA cm⁻², the voltage profile suggested an inhomogeneous current distribution, which got accelerated at 1 mA cm⁻² with an erratic asymmetric voltage profile. The high densification enabled the solid electrolyte to prevent the micro-short-circuit or complete short-circuit in the symmetric cell. At 0.2 mA cm⁻², the long-term cycling was tested to examine the interface stability (Figure 4(b)). The voltage profile maintained the flatness, indicating a uniform lithium plating/stripping onto/from the metal surface.

The HE-LSZT sample was employed as the solid electrolyte to demonstrate the application of a high-voltage NMC811 cathode in conjunction with a lithium metal anode. A PVDF-HFP/LiTFSI buffer layer was sandwiched between Li and HE-LSZT, whereas a liquid electrolyte drop was used at the NMC811-HE-LSZT interface. The impedance data is presented in Figure 4(c), where the abscissa and ordinate axes present the real and imaginary parts of the impedance values, along with the modeled data using an electrical equivalent circuit given in Figure 4(c) inset. The total

resistance of the full cell was found to be around $\sim 1104 \Omega$ ($R_E \sim 118 \Omega$, $R_1 \sim 156 \Omega$, $R_2 \sim 830 \Omega$). The electrolyte resistance and low-frequency diffusive behavior are given by R_E and Q_D , respectively, while the overlapped semicircular arcs are represented by $Q_1||R_1$ and $Q_2||R_2$. The high-frequency and mid-frequency impedance responses are ascribed to the SEI and charge transfer during redox processes.³⁵

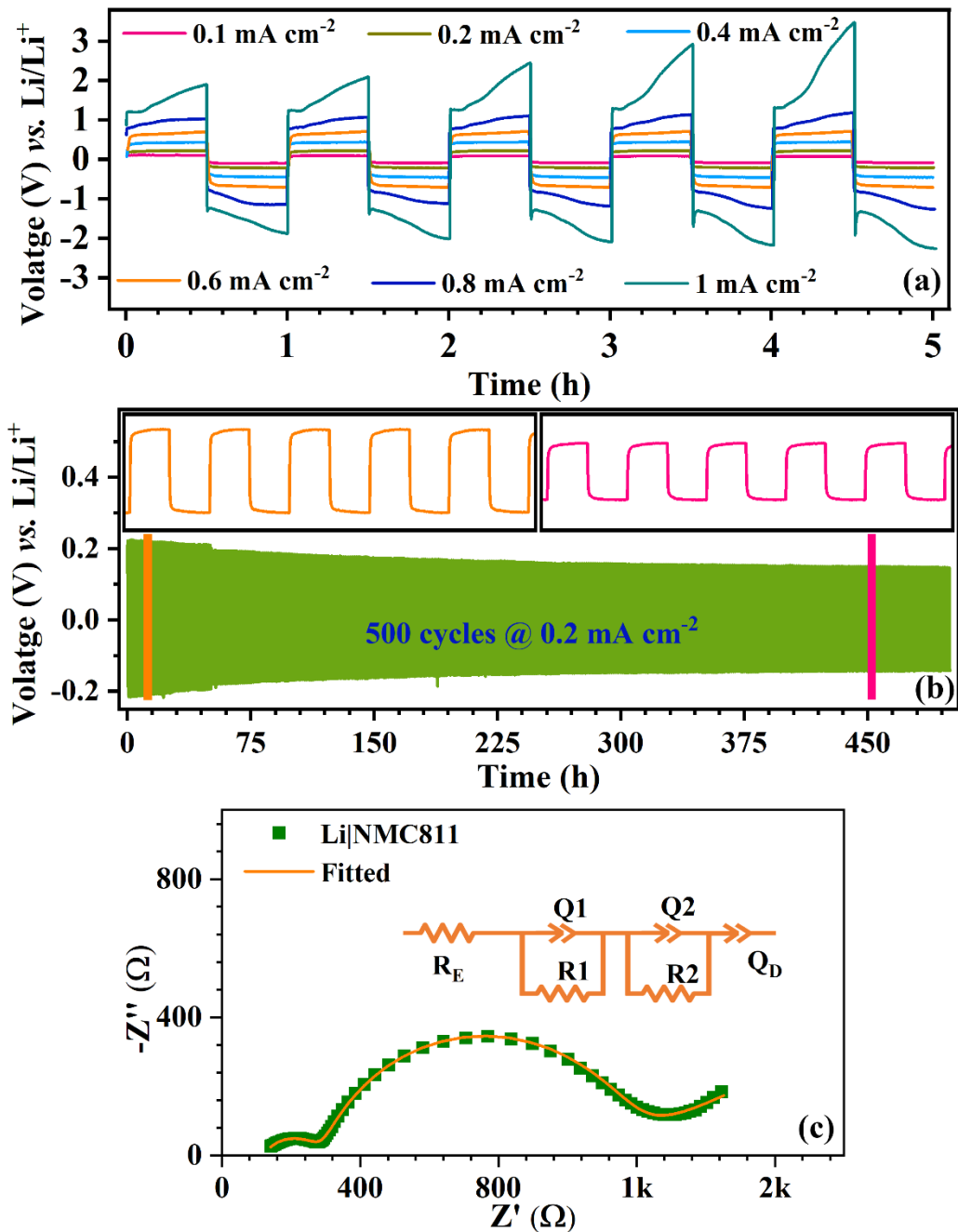


Figure 4: (a) The room temperature galvanostatic curves indicating lithium plating-stripping in Li| HE-LSZT |Li cell with buffer layer at different current densities. (b) The room temperature galvanostatic curves indicate lithium plating-stripping in Li| HE-LSZT |Li cell with a buffer layer at a current of 0.05 mA cm⁻² for 500 h. (c) Room temperature Nyquist plot of Li| |NMC cells with buffer layer. (inset displays the equivalent circuit used for fitting the impedance data). The scattered symbol and the pink line represent the experimental and fitted data, respectively.

As shown in Figure 5(a), the LiFePO_4 cell demonstrated a specific capacity of about 149 mAh g^{-1} at $C/10$ (C-rates are estimated assuming the theoretical specific capacity of LiFePO_4). This decreased to $\sim 138 \text{ mAh g}^{-1}$ (at $\sim C/5$), $\sim 125 \text{ mAh g}^{-1}$ (at $\sim C/3$), $\sim 101 \text{ mAh g}^{-1}$ (at $1C$), and $\sim 62 \text{ mAh g}^{-1}$ (at $\sim 2C$). Both capacity and energy efficiency decreased as current density increased. In addition, Figure 5(b) illustrates that the LiFePO_4 cells were charged-discharged at a constant current density ($1C$) to confirm the long cycling stability seen in lithium symmetric cells. It retained almost 99% of the capacity of the 1st cycle after 100 cycles. The excellent cycling stability could be attributed to the excellent ionic conductivity of the solid electrolyte along with the high cyclability of LiFePO_4 cathode materials. To showcase the application of the fabricated solid electrolyte in conjunction with high-energy cathode materials, the NMC811 cells were tested at different current densities along with a long cycling test. The NMC811 cell exhibited a specific capacity of $\sim 164 \text{ mAh g}^{-1}$ at $0.1C$ (C-rates are calculated assuming the practical specific capacity of NMC811 $\sim 200 \text{ mAh g}^{-1}$), which reduced to $\sim 140 \text{ mAh g}^{-1}$ at $\sim C/3$ and $\sim 112 \text{ mAh g}^{-1}$ at $\sim C/2$, as depicted in Figure 5(c). With the increase in current density, both the capacity and energy efficiency declined. Further, to affirm the long cycling stability demonstrated in lithium symmetric cells, the NMC811 cells were charged-discharged at a constant current density ($C/2$), as shown in Figures 5(d) and 5(e). As the number of cycles increased, the capacity degraded with a widened gap between the charge-discharge potentials, which can be devoted to the continuous growth of the SEI layer and cracking in NMC811 active cathode materials. The columbic efficiency of the cells remained at $\sim 99.99 \%$, indicating very low electronic conductivity of the ceramic sample, as discussed before.

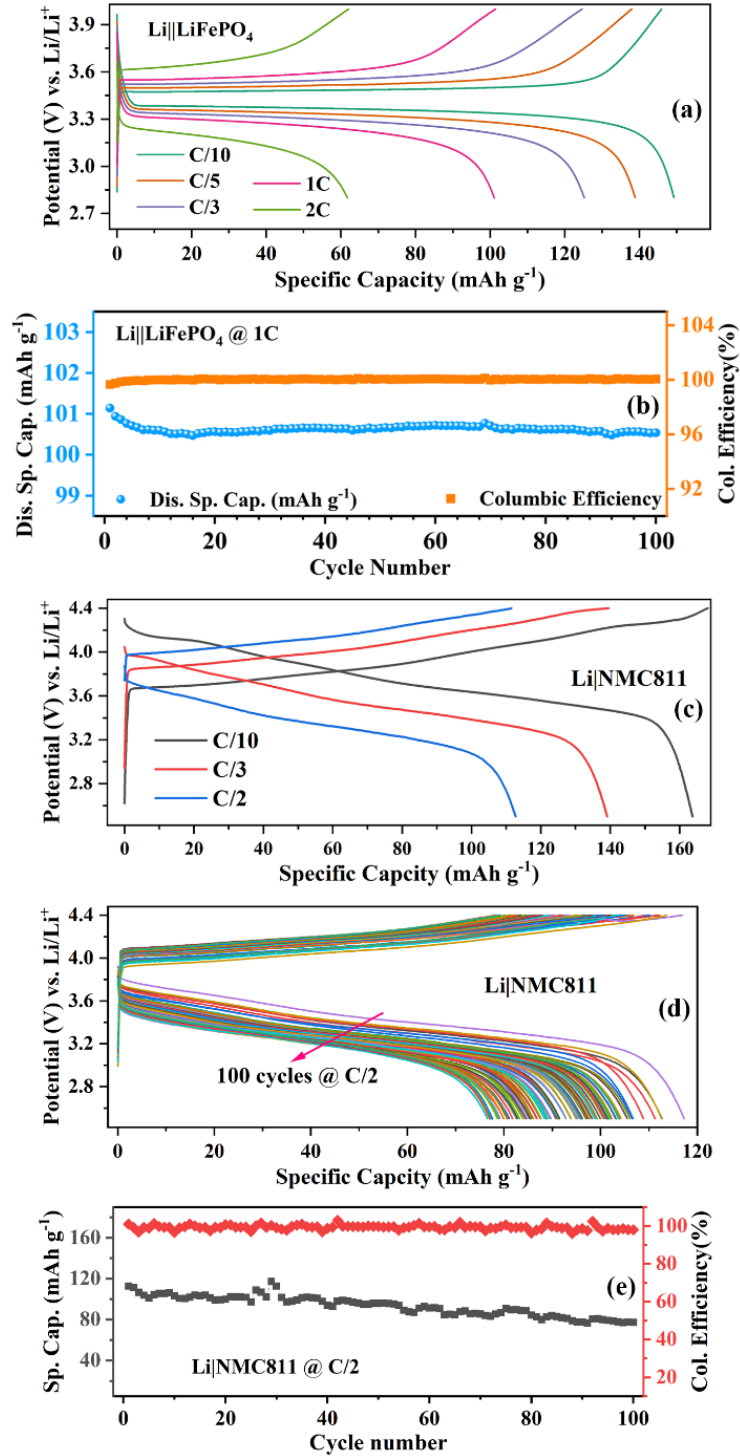


Figure 5: (a) The charge-discharge curves of Li|LiFePO₄ cells with buffer layer at different C-rates cycled at room temperature. (b) Room temperature long cycling data of Li|LiFePO₄ cells with buffer layer at 1C. (c) The charge-discharge curves of Li|NMC811 cells with buffer layer at different C-rates cycled at room temperature. (d) Galvanostatic charge-discharge curves of Li|NMC811 cells with buffer layer at C/2. (e) Room temperature long cycling data of Li|NMC811 cells with buffer layer at C/2.

In conclusion, a high entropy NASICON-type material with a rhombohedral phase exhibited excellent RT total conductivity of $\sim 1.42 \times 10^{-4} \text{ S cm}^{-1}$ with an activation energy of $\sim 0.33 \text{ eV}$. The samples achieved an excellent relative density of $\sim 94 \%$ by conventional sintering, and no cracks were observed in the microstructure. The symmetric cells with PVDF-HFP/LiTFSI buffer layer were tested at 0.2 mA cm^{-2} for 500 cycles (each cycle: 30 minutes charge and 30 minutes discharge) without any sign of short-circuit. The full cells fabricated using LiFePO_4 delivered $\sim 99\%$ of its capacity after 100 cycles at 1C rate, while the full cells with NMC811 as the cathode delivered a specific capacity of $\sim 140 \text{ mAh g}^{-1}$ at C/3 rate. The satisfactory rate performance and long cycle performance demonstrate the stability and feasibility of implementing high-performance NASICON-structured quasi-solid-state lithium batteries.

Conflicts of Interest

There are no conflicts of interest to declare.

Data Availability

Data will be made available on request.

Credit author statement

Asish Kumar Das: Conceptualisation, Methodology, Investigation, Funding acquisition, Data curation, Formal analysis, Writing - Original Draft; **Pratiksha Gami:** Writing - Review & Editing; **Hari Narayanan Vasavan:** Writing - Review & Editing; **Samridhi Saxena:** Writing - Review & Editing; **Neha Dagar:** Writing - Review & Editing; **Sonia Deswal:** Writing - Review & Editing; **Pradeep Kumar:** Writing - Review & Editing; **Sunil Kumar:** Conceptualisation, Methodology, Funding acquisition, Supervision, Resources, Project administration, Validation, Writing - Review & Editing.

Acknowledgments

The author (AKD) thanks the Ministry of Education, Government of India, for the Prime Ministers Research Fellowship (PMRF) (PMRF ID - 2102737). The authors gratefully acknowledge the Science and Engineering Research Board (SERB), Government of India (Grant No. CRG/2021/005548) and Ministry of Education (MoE), Government of India (Grant No. MoE-STARS/STARS-2/2023-0365).

References

1. Sun, Y.-K., Promising All-Solid-State Batteries for Future Electric Vehicles. *ACS Energy Lett.* **2020**, *5* (10), 3221.
2. Goodenough, J. B.; Park, K.-S., The Li-Ion Rechargeable Battery: A Perspective. *J. Am. Chem. Soc.* **2013**, *135* (4), 1167.
3. Evarts, E. C., Lithium batteries: To the limits of lithium. *Nature* **2015**, *526* (7575), S93.
4. Diouf, B.; Pode, R., Potential of lithium-ion batteries in renewable energy. *Renew. Energ.* **2015**, *76*, 375.
5. Jiang, Z.; Yu, C.; Chen, S.; Wei, C.; Liao, C.; Wu, Z.; Chen, S.; Cheng, S.; Xie, J., Ag/Br dual-doped Li₆PS₅Br electrolyte with superior conductivity for all-solid-state batteries. *Scripta Mater.* **2023**, *227*, 115303.
6. Liao, C.; Yu, C.; Chen, S.; Wei, C.; Miao, X.; Cheng, S.; Xie, J., Hunting highly conductive Li₆PS₅I electrolyte via Sn-Cl dual doping for solid-state batteries. *Scripta Mater.* **2023**, *226*, 115219.
7. Park, S.-J.; Rajagopal, R.; Subramanian, Y.; Ryu, K.-S., High ionic conductivity lithium superionic halogen-rich argyrodite synthesized by liquid-phase technique. *Scripta Mater.* **2024**, *238*, 115726.
8. Subramanian, Y.; Rajagopal, R.; Ryu, K.-S., High ionic-conducting Li-argyrodites synthesized using a simple and economic liquid-phase approach and their application in all solid-state-lithium batteries. *Scripta Mater.* **2021**, *204*, 114129.
9. Kim, Y.; Choi, S., Investigating stacking variations in Li₃InCl₆ crystal structure and their influence on solid electrolyte properties. *Acta Mater.* **2024**, *276*, 120135.
10. Lee, Y.; Kim, Y.-H.; An, J.-H.; Lee, J.-C., Ionic conduction mechanisms in 70Li₂S–30P₂S₅ type electrolytes: experimental and atomic simulation studies. *Acta Mater.* **2022**, *235*, 118106.
11. Liu, H.; Liang, Y.; Wang, C.; Li, D.; Yan, X.; Nan, C.-W.; Fan, L.-Z., Priority and Prospect of Sulfide-Based Solid-Electrolyte Membrane. *Adv. Mater.* **2023**, *35* (50), 2206013.
12. Li, S.; Lu, J.; Geng, Z.; Chen, Y.; Yu, X.; He, M.; Li, H., Solid Polymer Electrolyte Reinforced with a Li_{1.3}Al_{0.3}Ti_{1.7}(PO₄)₃-Coated Separator for All-Solid-State Lithium Batteries. *ACS Appl. Mater. Interfaces* **2022**, *14* (1), 1195.
13. Sung, B.-J.; Didwal, P. N.; Verma, R.; Nguyen, A.-G.; Chang, D. R.; Park, C.-J., Composite solid electrolyte comprising poly(propylene carbonate) and Li_{1.5}Al_{0.5}Ge_{1.5}(PO₄)₃ for long-life all-solid-state Li-ion batteries. *Electrochim. Acta* **2021**, *392*, 139007.
14. Wang, J.; He, T.; Yang, X.; Cai, Z.; Wang, Y.; Lacivita, V.; Kim, H.; Ouyang, B.; Ceder, G., Design principles for NASICON super-ionic conductors. *Nat. Commun.* **2023**, *14* (1), 5210.
15. Das, A. K.; Badole, M.; Vasavan, H. N.; Saxena, S.; Gami, P.; Deswal, S.; Kumar, P.; Kumar, S., Enhancing room temperature performance of solid-state lithium cell via a facile solid electrolyte-cathode interface design. *Mater. Today Sustain.* **2024**, *26*, 100758.

16. Das, A. K.; Badole, M.; Vasavan, H. N.; Saxena, S.; Gami, P.; Kumar, S., Highly conductive ceramic-in-polymer composite electrolyte enabling superior electrochemical performance for all-solid-state lithium batteries. *Ceram. Int.* **2023**, *49* (18), 29719.
17. Gami, P.; Badole, M.; Vasavan, H. N.; Das, A. K.; Saxena, S.; Kumar, S., Y-Doped $\text{LiZr}_2(\text{PO}_4)_3$ in a PVDF-HFP Composite Electrolyte for Solid-State Li-Metal Batteries. *ACS Applied Engineering Materials* **2024**, *2* (5), 1278.
18. Kumar, S.; Balaya, P., Improved ionic conductivity in NASICON-type Sr^{2+} doped $\text{LiZr}_2(\text{PO}_4)_3$. *Solid State Ion.* **2016**, 296, 1.
19. Ouyang, B.; Zeng, Y., The rise of high-entropy battery materials. *Nat. Commun.* **2024**, *15* (1), 973.
20. Wu, B.; Hou, G.; Kovalska, E.; Mazanek, V.; Marvan, P.; Liao, L.; Dekanovsky, L.; Sedmidubsky, D.; Marek, I.; Hervoches, C.; Sofer, Z., High-Entropy NASICON Phosphates ($\text{Na}_3\text{M}_2(\text{PO}_4)_3$ and NaMPO_4O_x , M = Ti, V, Mn, Cr, and Zr) for Sodium Electrochemistry. *Inorg. Chem.* **2022**, *61* (9), 4092-4101.
21. Li, M.; Sun, C.; Ni, Q.; Sun, Z.; Liu, Y.; Li, Y.; Li, L.; Jin, H.; Zhao, Y., High Entropy Enabling the Reversible Redox Reaction of $\text{V}^{4+}/\text{V}^{5+}$ Couple in NASICON-Type Sodium Ion Cathode. *Adv. Energy Mater.* **2023**, *13* (12), 2203971.
22. Ahsan, M. T.; Qiu, D.; Ali, Z.; Fang, Z.; Zhao, W.; Shen, T.; Hou, Y., Unraveling the Fast Na Diffusion Kinetics of NASICON at High Voltage via High Entropy for Sodium-Ion Battery. *Adv. Energy Mater.* **2024**, *14* (4), 2302733.
23. Li, M.; Sun, C.; Yuan, X.; Li, Y.; Yuan, Y.; Jin, H.; Lu, J.; Zhao, Y., A Configuration Entropy Enabled High-Performance Polyanionic Cathode for Sodium-Ion Batteries. *Adv. Funct. Mater.* **2024**, *34* (21), 2314019.
24. Li, Y.; Sun, C.; Sun, Z.; Li, M.; Jin, H.; Zhao, Y., Boosting Na-O Affinity in $\text{Na}_3\text{Zr}_2\text{Si}_2\text{PO}_{12}$ Electrolyte Promises Highly Rechargeable Solid-State Sodium Batteries. *Adv. Funct. Mater.* **2024**, 2403937.
25. Zeng, Y.; Ouyang, B.; Liu, J.; Byeon, Y.-W.; Cai, Z.; Miara, L. J.; Wang, Y.; Ceder, G., High-entropy mechanism to boost ionic conductivity. *Science* **2022**, *378* (6626), 1320.
26. Wang, M. J.; Wolfenstine, J. B.; Sakamoto, J., Mixed Electronic and Ionic Conduction Properties of Lithium Lanthanum Titanate. *Adv. Funct. Mater.* **2020**, *30* (10), 1909140.
27. Noda, Y.; Nakano, K.; Otake, M.; Kobayashi, R.; Kotobuki, M.; Lu, L.; Nakayama, M., Research Update: Ca doping effect on the Li-ion conductivity in NASICON-type solid electrolyte $\text{LiZr}_2(\text{PO}_4)_3$: A first-principles molecular dynamics study. *APL Mater.* **2018**, *6* (6), 060702.
28. Yang, Y.; Chen, W.; Lu, X., Coordination Li diffusion chemistry in NASICON $\text{Li}_{1.5}\text{Al}_{0.5}\text{Ge}_{1.5}(\text{PO}_4)_3$ solid electrolyte. *Solid State Ion.* **2022**, *381*, 115947.
29. Courbaron, G.; Nuernberg, R. B.; Sevillano, J. S.; Chung, U. C.; Duttine, M.; Labrugère-Sarroste, C.; Olchowka, J.; Carlier, D.; Delpuech, N.; Croguennec, L., Multi-scale characterization of submicronic NASICON-type solid electrolyte $\text{Li}_{1.3}\text{Al}_{0.3}\text{Ti}_{1.7}(\text{PO}_4)_3$ degraded by spark plasma sintering. *J. Alloys Compd.* **2024**, *985*, 174062.

30. Pu, X.; Cheng, X.; Yan, Q.; Lin, Y.; Yan, R.; Yang, R.; Zhu, X., NASICON-type Ta⁵⁺ substituted LiZr₂(PO₄)₃ with improved ionic conductivity as a prospective solid electrolyte. *Ceram. Int.* **2024**, *50* (6), 9007-9015.
31. Gami, P.; Badole, M.; Vasavan, H. N.; Das, A. K.; Saxena, S.; Dagar, N.; Srihari, V.; Kumar, S., NASICON-type medium entropy Li_{1.5}Sn_{1.0}Al_{0.5}Zr_{0.5}(PO₄)₃ electrolyte for solid state Li metal batteries. *J. Power Sources* **2024**, *618*, 235214.
32. Chen, K.-H.; Wood, K. N.; Kazyak, E.; LePage, W. S.; Davis, A. L.; Sanchez, A. J.; Dasgupta, N. P., Dead lithium: mass transport effects on voltage, capacity, and failure of lithium metal anodes. *J. Mater. Chem. A* **2017**, *5* (23), 11671.
33. Chen, X. R.; Yan, C.; Ding, J. F.; Peng, H. J.; Zhang, Q., New insights into “dead lithium” during stripping in lithium metal batteries. *J. Energy Chem.* **2021**, *62*, 289.
34. Zhou, M.; Liao, Y.; Li, L.; Xiong, R.; Shen, G.; Chen, Y.; Huang, T.; Li, M.; Zhou, H.; Zhang, Y., Unraveling the heterogeneity of solid electrolyte interphase kinetically affecting lithium electrodeposition on lithium metal anode. *J. Energy Chem.* **2023**, *85*, 181.
35. Das, A. K.; Badole, M.; Vasavan, H. N.; Saxena, S.; Gami, P.; Dagar, N.; Kumar, S., Integrated cathode-electrolyte (Li_{6.55}La₃Zr_{1.55}Ta_{0.45}O₁₂/PEO-LiTFSI) architecture driven excellent performance of solid-state lithium metal batteries. *J. Energy Storage* **2024**, *94*, 112452.

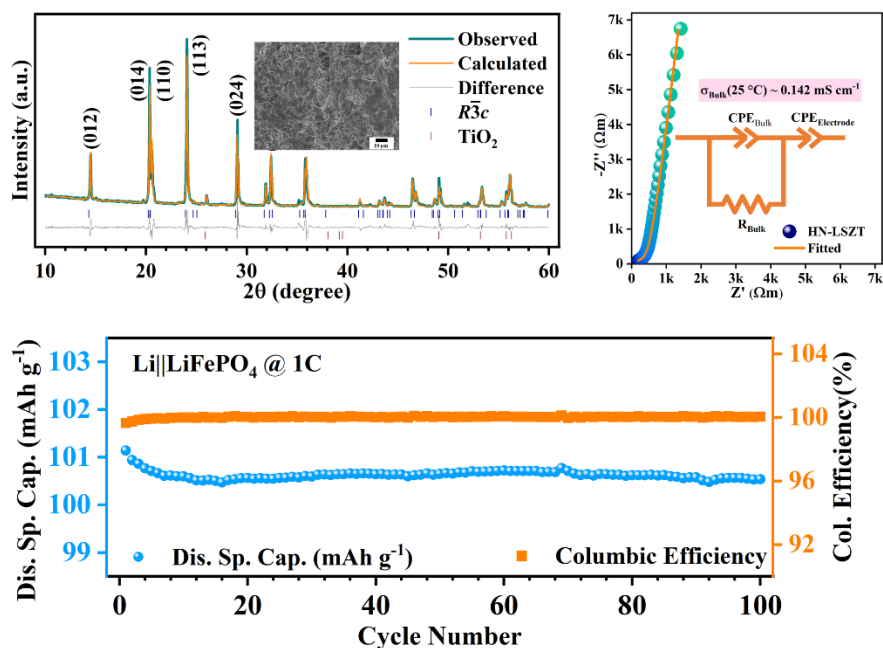


Table of Contents (TOC)

[Supporting Information]

Advancing High-Energy Solid-State Batteries with High-Entropy NASICON-type Solid Electrolytes

Asish Kumar Das^a, Pratiksha Gami^a, Hari Narayanan Vasavan^a, Samriddhi Saxena^a, Neha Dagar^a, Sonia Deswal^b, Pradeep Kumar^b, Sunil Kumar^{a,*}

^aDepartment of Metallurgical Engineering and Materials Science, Indian Institute of Technology Indore, Simrol, 453552, India

^bSchool of Physical Sciences, Indian Institute of Technology Mandi, Himachal Pradesh, 175005, India

*Corresponding author E-mail: sunil@iiti.ac.in

1. Experimental method

1.1 HE-LSZT synthesis

Stoichiometric amounts of lithium hydroxide (LiOH), tin (IV) chloride pentahydrate (SnCl₄·5H₂O), zirconium oxide (ZrO₂), titanium dioxide (TiO₂), aluminium nitrate nonahydrate (Al(NO₃)₃·9H₂O), scandium oxide (Sc₂O₃), yttrium oxide (Y₂O₃), and ammonium dihydrogen phosphate (NH₄·H₂PO₄) raw materials were measured. To compensate for the evaporation of Li₂O at high temperatures, 10 wt.% of excess LiOH was added. The mixture underwent ball milling for 12 h, then heated at 600 °C for 12 h to facilitate thermal decomposition. Subsequently, the obtained powders were ball milled again for 12 h and then dried. The resulting powders were added to a die and pressed into ceramic pellets of 10 mm diameter under a uniaxial pressure of ~ 200 MPa. Finally, the green ceramic pellets were reactive sintered at 1200 °C for 12 h.

1.2 Buffer layer preparation

P(VDF-HFP) and LiTFSI (in the wt. ratio of 2.5:1) were dissolved in a DMF solvent, followed by stirring for 6 h. This transparent solution was cast onto the ceramic surface facing the lithium metal and dried at 60 °C for 24 h in a vacuum oven to eliminate the solvent. The resulting dried P(VDF-HFP)/LiTFSI buffer layer coated on the ceramic sample was subsequently stored in a glove box filled with Argon for the fabrication of coin cells.

1.3 Coin cell fabrication

The symmetric lithium cells named Li|HE-LSZT|Li cells were fabricated with lithium metal as the electrodes with and without a buffer layer. For a full cells' fabrication, LiFePO₄ and NMC811 cathode slurry (solvent: NMP, weight ratio of PVDF: Ketjen black: active material ~ 10: 10: 80) coated on an aluminium current collector was kept in a vacuum oven (temperature: 120 °C, dwelling time: 24 h). The punched circular cathodes (diameter: 1 cm) were transferred into the Ar-filled Glovebox. The active material loading of LiFePO₄ and NMC811 cathodes are ~ 1-2 mg cm⁻² and ~ 5 mg cm⁻², respectively. During the fabrication of full cells, a 5 μL of liquid electrolyte 1M LiPF₆ in EC: DMC (1:1 vol. ratio) was employed at the HE-LSZT-cathode interface.

1.4 Characterization techniques

X-ray diffraction (XRD) analysis was conducted using an Empyrean X-ray diffractometer with Cu-K α radiation covering the 2 θ range of 10° to 60°. Rietveld refinement was used to estimate the crystallographic parameters from the XRD data (employing the TOPAS academic version 6 software). The relative density of the sintered sample was determined by Archimedes' method. The microstructural characteristics of the prepared sample were investigated using a JEOL-7610+ field emission scanning electron microscope (FE-SEM). Impedance data were obtained utilizing an NF Corp. LCR meter (Model: ZM2376) in 1 Hz - 1 MHz range on sintered HE-LSZT pellets with silver electrodes painted on either side, as well as the lithium symmetric cells and full cells.

X-ray photoelectron spectroscopy (XPS) data were obtained using a ThermoFisher Scientific (Naxsa base) instrument (Al K α X-ray source). DC polarisation tests were carried out in Ag| HE-LSZT |Ag cells, along with cyclic voltammetry (CV) in symmetric Li| HE-LSZT |Li cells and linear sweep voltammetry (LSV) in Li| HE-LSZT |Ag cells using a Keithley Source Meter Unit (model 2450-EC). Galvanostatic charge-discharge (GCD) measurements were also carried out on lithium symmetric and full cells in a Neware CT-2001A battery tester. All characterizations except impedance measurements were performed at room temperature (25 °C).

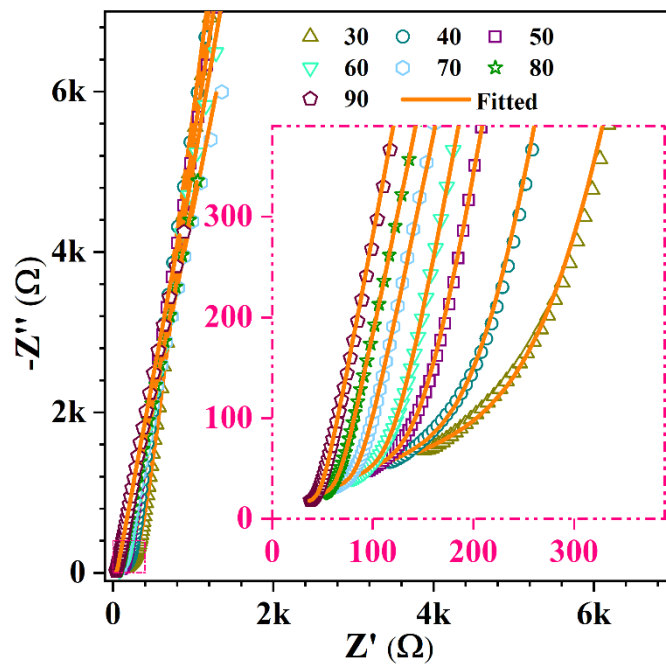


Figure S1: Nyquist plots of HE-LSZT sample at different temperatures (°C).

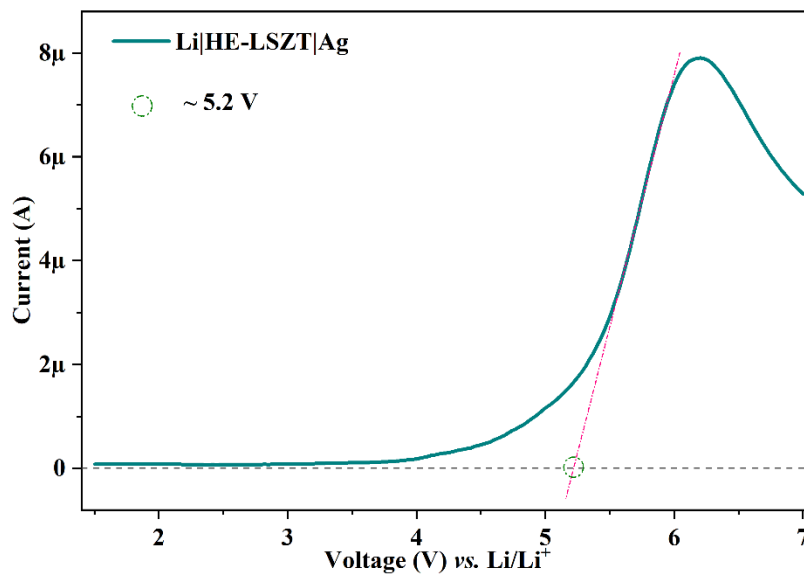


Figure S2: Linear sweep voltammetry result of Li|HE-LSZT|Ag cell.

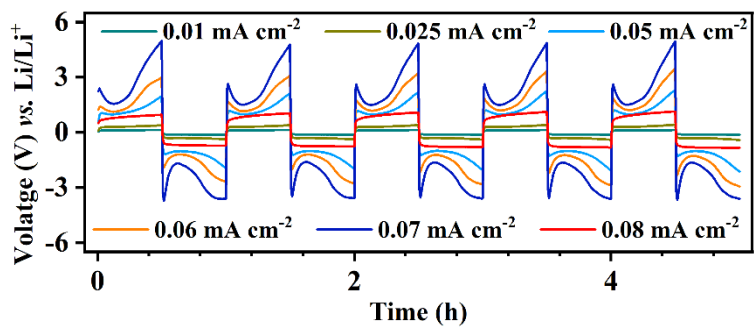


Figure S3: Lithium plating-stripping voltage profile of Li|HE-LSZT|Li symmetric cells without any buffer layer at different current densities.